Effects of Solid Particles at Varying Concentrations on Hydrodynamic Cavitation Evolution in a Nozzle

D. Wang[1,2], W. G. Zhao[1†] and X. D. Han[3]

[1] *College of Energy and Power Engineering, Lanzhou University of Technology, Lanzhou 730050, China*
[2] *School of Mechanical and Electrical Engineering, Lanzhou Vocational Technical College, Lanzhou 730070, China*
[3] *Norinco Group Testing and Research Institute, Xi'an 710116, China*

†*Corresponding Author Email: zhaowg@zju.edu.cn*

ABSTRACT

This study investigated the effects of solid particles at varying concentrations on hydrodynamic cavitation within a nozzle in a solid particle-pure water-hydrodynamic cavitation flow system. Concentrations ranged from 5% to 10%, and mean diameters varied from 0.0015 mm to 0.040 mm. The Zwart-Gerber-Belamri cavitation model, originally developed for pure water-hydrodynamic cavitation flow, was adapted for the solid particle-pure water-hydrodynamic cavitation flow scenario. A novel algorithm integrating solid, liquid, and vapor phases was developed to facilitate numerical simulations of this flow. Comparisons were made between the vapor contents in solid particle-pure water-hydrodynamic cavitation flow under different concentrations and those in pure water-hydrodynamic cavitation flow to establish variation patterns. Solid particles consistently promoted cavitation evolution across all concentration conditions. However, the range of mean diameter promoting cavitation decreased with increasing concentration. The study analyzed variations in solid particle properties, flow fields, and the forces acting on solid particles to elucidate the underlying mechanisms. Solid particles induced a greater number of cavitation nuclei. In the solid particle-pure water-hydrodynamic cavitation flow, the maximum and minimum slip velocities, as well as the maximum and minimum turbulent kinetic energies, were higher than those in pure water-hydrodynamic cavitation flow, establishing these factors as primary influencers. Conversely, the Saffman lift force was relatively small, rendering its effects as secondary. The combined effects of these factors contributed to the distinctive evolution of hydrodynamic cavitation within the nozzle.

1. INTRODUCTION

Cavitation, a type of multiphase flow, frequently occurs in various fluid machinery, such as pumps and hydro turbines, when the local pressure drops below the saturated vapor pressure (Ranade et al., 2022).

The evolution of cavitation is significantly influenced by both internal and external factors (Das & Chatterjee, 2023). In rivers containing solid particles, these particles substantially affect cavitation development. This situation leads to the formation of a solid particle-pure water-hydrodynamic cavitation flow (SP-PW-HCF), which constitutes a solid-liquid-vapor three-phase flow with mass transfer and phase change (Han et al., 2019). This flow is more complex than both the solid particle-pure water flow (SP-PWF) (Zhou et al., 2020; Zhang et al., 2023; Zhu et al., 2023) and the pure water-hydrodynamic cavitation flow (PW-HCF).

In SP-PWF, solid particles cause solid particle abrasion (SPA) (Chen et al., 2015; Liu et al., 2016; Peng et al., 2021, Lv et al., 2023; Song et al., 2016; Koirala et al., 2017; Jin et al., 2023). In PW-HCF, cavitation erosion (CE) occurs (Kang et al., 2021; Bel Hadj Taher et al., 2022). In SP-PW-HCF, both SPA and CE contribute to the damage, resulting in a combined destructive effect that differs from SPA and CE alone (Sun et al., 2023).

Research on the combined damage and interaction of SPA and CE with various materials and fluid-handling devices, as well as corresponding mitigation methods, is extensive. Some notable studies include:

Su et al. (2023) employed carbon steel to conduct vibratory erosion tests, examining the effects of particle size distribution on CE. They observed that different size distributions led to varied erosion behaviors. Stella and Alcivar (2019) investigated the effects of fine alumina particles on CE, analyzing variations in mass loss rate, surface hardening, and microstructural morphology to assess the role of particles. Romero et al. (2019) explored the joint destruction of SPA and CE on AISI 316 stainless steel with varying particle diameters and concentrations, revealing complex laws under different conditions. Chen et al. (2021) utilized ultrasonic vibration cavitation equipment and underwater low-voltage electric discharge apparatus to study the effects of different sandy particle diameters and concentrations on CE. They observed that increased mean diameter and concentration exacerbated the destruction caused by CE. Peng et al. (2021) conducted experiments to examine the combined destruction characteristics of CE and SPA with SiO_2 at various concentrations, noting significant increases in destruction of sandstone, shale, and granite. Lin et al. (2020) performed numerical studies on the combined damage of SPA and CE in a centrifugal pump, finding that particle concentration had a more significant impact on CE than mean diameter. They also noted that cavitation and particles influenced each other. Xu et al. (2019) investigated CE characteristics in a multistage slurry pump used in deep-sea mining processes, finding significant effects of both particle size and concentration on CE. Krella et al. (2020) conducted experiments to assess the effects of micro Ti particles in resisting CE of Mg-*x*Ti composites, with Mg-2.5Ti exhibiting the best resistance performance. Hegde et al. (2023) developed a new coating by integrating anodized layers with superhydrophobic sol-gel coatings to enhance resistance against SPA and CE in aluminum alloys.

The research findings regarding SPA and CE are diverse, with varying conclusions based on different conditions. The primary reason for these discrepancies is the insufficient understanding of the mechanisms and laws governing SP-PW-HCF.

Therefore, based on the distribution characteristics of concentration and mean diameter in sediment samples from the Yellow River and Yangtze River (Figs. 1 and 2), appropriate concentrations and mean diameters were selected. Concentrations ranged from 5% to 10%, and mean diameters varied from 0.0015 mm to 0.040 mm.

This study constructed a cavitation model for SP-PW-HCF and developed a new algorithm for coupling solid, liquid, and vapor phases. Numerical simulations were conducted for SP-PW-HCF at various concentrations and mean diameters, and for PW-HCF in the nozzle. The vapor contents of SP-PW-HCF and PW-HCF were compared to establish the effects of solid particle concentration. The study also analyzed variations in cavitation nuclei, slip velocity, turbulent kinetic energy, and Saffman lift force to reveal the underlying mechanisms.

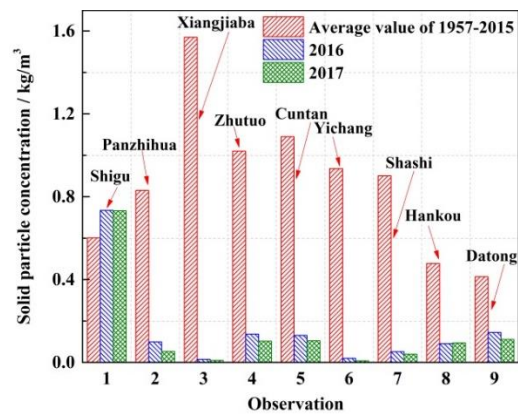The findings of this study can provide essential theoretical guidance and practical references for
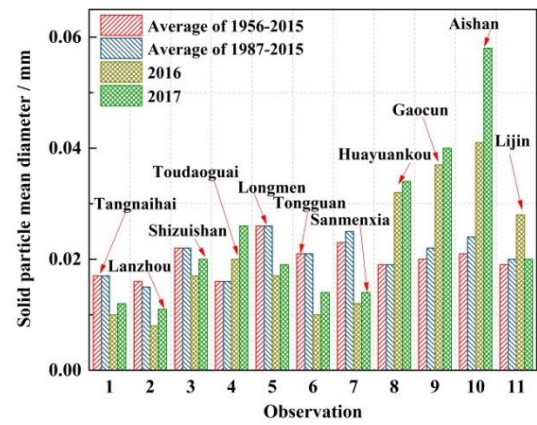
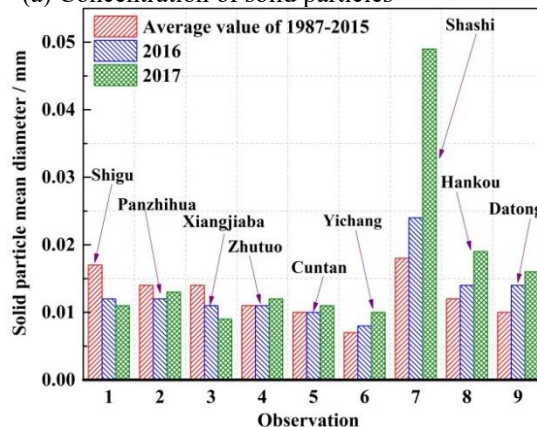(a) Concentration of solid particles
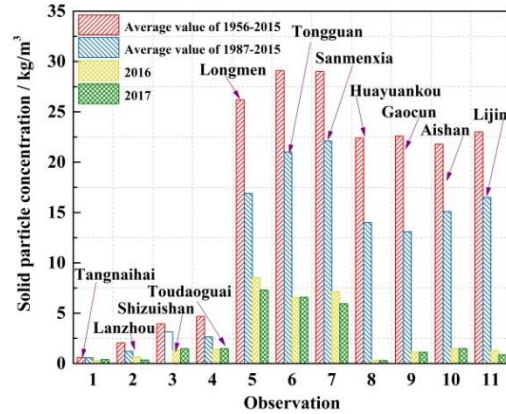
(b) Mean diameter of solid particles

Fig. 1 Distribution characteristics of solid particles in various observations of Yellow River

(a) Concentration of solid particles

(b) Mean diameter of solid particles

Fig. 2 Distribution characteristics of solid particles in various observations of Yangtze River

understanding the joint destruction of SPA and CE in hydraulic machinery operating in particle-laden rivers.

2. MATHEMATICAL METHOD

2.1 Fundamental Equations

ANSYS-Fluent was employed to perform the numerical simulation of SP-PW-HCF. It was a transient calculation. The mixture model was used to solve the multiphase flow. Water served as the primary phase, while vapor and solid particles were considered secondary phases. Cavitation occurred between water and vapor. Solid particles had significant effects on cavitation evolution.

Water and vapor were treated as homogeneous fluids, having identical pressure and velocity fields. Solid particles, due to their exceptionally small mean diameter, were treated as a pseudo-fluid.

The fundamental equations used in this simulation included the continuity equation, momentum equation, transport equation, and relative velocity equation (Mueller, 2020), expressed as follows:

$$\frac{\partial \rho_m}{\partial t} + \frac{\partial (\rho_m u_j)}{\partial x_j} = 0 \tag{1}$$

$$\frac{\partial (\rho_m u_i)}{\partial t} + \frac{\partial (\rho_m u_i u_j)}{\partial x_j} = -\frac{\partial p}{\partial x_i} + \frac{\partial}{\partial x_j}\left(\mu_m \frac{\partial u_i}{\partial x_j}\right) \tag{2}$$

$$\frac{\partial \rho_l \alpha_l}{\partial t} + \frac{\partial (\rho_l \alpha_l u_j)}{\partial x_j} = R = R_e - R_c \tag{3}$$

$$\frac{\partial \rho_v \alpha_v}{\partial t} + \frac{\partial (\rho_v \alpha_v u_j)}{\partial x_j} = -R \tag{4}$$

$$\frac{\partial \rho_s \alpha_s}{\partial t} + \frac{\partial (\rho_s \alpha_s u_j)}{\partial x_j} = 0 \tag{5}$$

$$\mathbf{v}_{pq} = \mathbf{v}_p - \mathbf{v}_q \tag{6}$$

where ρ_m, ρ_l, ρ_v, and ρ_s denote the densities of the mixture, water, vapor, and solid particles, respectively. u denotes the velocity of the mixture, and x represents the coordinate. The indices i and j denote different directions in the Cartesian coordinate system (values are 1, 2, and 3). α_l, α_v, and α_s are the concentrations of water, vapor, and solid particles, respectively. p denotes the local pressure. μ_m denotes the viscosity of the mixture. R_e and R_c represent evaporation and condensation source terms, respectively, with R denoting the total. V_{pq} denote the relative velocity between the secondary and primary phases. V_p denotes the velocity of the secondary phase (vapor or solid particles), and V_q denotes the velocity of the primary phase (water). t denotes the time.

ρ_m was calculated as follows:

$$\rho_m = \rho_l \alpha_l + \rho_v \alpha_v + \rho_s \alpha_s \tag{7}$$

Similarly, μ_m was calculated as follows:

$$\mu_m = \mu_l \alpha_l + \mu_v \alpha_v + \mu_s \alpha_s \tag{8}$$

where μ_l denotes the viscosity of water, μ_v denotes the viscosity of vapor, and μ_s denotes the viscosity of solid particles.

The bulk density ρ_s of solid particles was defined as the mass per unit volume under natural packing conditions:

$$\rho_s = \frac{m_s}{v_s} \tag{9}$$

where m_s denotes the mass of solid particles, and v_s denotes the corresponding volume.

The viscosity of solid particles, μ_s, was calculated as follows:

$$\mu_s = \mu_{s\text{-col}} + \mu_{s\text{-kin}} + \mu_{s\text{-fr}} \tag{10}$$

where $\mu_{s\text{-col}}$, $\mu_{s\text{-kin}}$, and $\mu_{s\text{-fr}}$ denote the collisional, kinetic, and optional frictional viscosities, respectively.

The collisional viscosity $\mu_{s\text{-col}}$ (Gidaspow et al., 1992) was calculated as follows:

$$\mu_{s\text{-col}} = \frac{4}{5}\alpha_s \rho_s d_s g_{0,ss}(1+e_{ss})\left(\frac{\Theta_s}{\pi}\right)^{1/2}\alpha_s \tag{11}$$

The kinetic viscosity $\mu_{s\text{-kin}}$ (Syamlal et al., 1993) was defined as follows:

$$\mu_{s\text{-kin}} = \frac{\alpha_s d_s \rho_s \sqrt{\Theta_s \pi}}{6(3-e_{ss})}\left[1+\frac{2}{5}(1+e_{ss})(3e_{ss}-1)\alpha_s g_{0,ss}\right] \tag{12}$$

where e_{ss} denotes the restitution coefficient for collisions, $g_{0,ss}$ represents the radial distribution function at contact, and Θ_s denotes the granular temperature.

The optional frictional viscosity $\mu_{s\text{-fr}}$ (Schaeffer, 1987) was defined as follows:

$$\mu_{s\text{-fr}} = \frac{p_s \sin\phi}{2\sqrt{I_{2D}}} \tag{13}$$

where p_s denotes the solid particle pressure, Φ denotes the internal friction angle, and I_{2D} denotes the deviatoric stress tensor second invariant.

For the numerical simulation of PW-HCF, Eqs. (1)-(4) were used. In this context, $\rho_{m\text{-}l\text{-}v}$ represents the mixture density, and $\mu_{m\text{-}l\text{-}v}$ denotes the mixture viscosity in PW-HCF:

$$\rho_m = \rho_l \alpha_l + \rho_v \alpha_v \tag{14}$$

$$\mu_m = \mu_l \alpha_l + \mu_v \alpha_v \tag{15}$$

2.2 Turbulence Model

A hybrid detached eddy simulation (DES) model (Spalart, 2009), based on the shear stress transport (SST) k-ω turbulence model (Menter, 1994), was employed to solve the turbulent flows of PW-HCF and SP-PW-HCF. During the numerical simulation, the y plus (y^+) value was maintained below 1.

2.2.1 SST k-ω Turbulent Model

The SST k-ω model integrates the benefits of both the k-ω model and k-ε models. It uses blending functions to determine action modes in different regions based on turbulent length scales. The k-ω model is applied in regions near the wall, while the k-ε model is used in areas farther from the wall:

$$\rho \frac{\partial k}{\partial t} + \rho \overline{u_j} \frac{\partial k}{\partial x_j} = P_k - \rho \beta_* \omega k + \frac{\partial}{\partial x_j}\left[\left(\mu + \frac{\mu_t}{\sigma_k}\right)\frac{\partial k}{\partial x_j}\right] \tag{16}$$

$$\rho \frac{\partial \omega}{\partial t} + \rho \overline{u_j} \frac{\partial \omega}{\partial x_j} = \alpha P_\omega - \rho \beta \omega^2 + \frac{\partial}{\partial x_j}\left[\left(\mu + \frac{\mu_t}{\sigma_\omega}\right)\frac{\partial \omega}{\partial x_j}\right] \\ + 2\rho(1 - F_B)\frac{1}{\sigma_{\omega_{out}}\omega}\frac{\partial k}{\partial x_j}\frac{\partial \omega}{\partial x_j} \tag{17}$$

where k represents the turbulent kinetic energy, and ω is the specific dissipation rate, quantifying the conversion of k into thermal internal energy per unit volume and time. P_k and P_ω are the production terms for turbulent kinetic energy and specific dissipation rate, respectively. F_B is the blending function, μ denotes the dynamic viscosity, and μ_t denotes the eddy viscosity. The constants are $\beta_* = 0.09$ and $\sigma_{\omega out} = 1.168$.

2.2.2 Detached Eddy Simulation

In DES based on the SST k-ω turbulence model, the general form of the length scale $l_{DES-SST}$ can be expressed as follows:

$$l_{DES-SST} = \min\left(l_{RANS-SST}, C_{DES-SST}\Delta\right) \tag{18}$$

where $l_{RANS-SST}$ denotes the length scale of the SST k-ω turbulence model, defined as follows:

$$l_{RANS-SST} = \frac{k^{1/2}}{(\beta^*\omega)} \tag{19}$$

where Δ represents the size of the maximum cell.

The empirical constant $C_{DES-SST}$ can be expressed as follows:

$$C_{DES-SST} = (1 - F_B)C_{DES-(k-\varepsilon)} + F_1 C_{DES-(k-\omega)} \tag{20}$$

where $C_{DES-(k-\varepsilon)} = 0.61$ and $C_{DES-(k-\omega)} = 0.78$.

2.3 Cavitation Model

2.3.1 Pure Water-Hydrodynamic Cavitation Flow

For the numerical simulation of pure water-hydrodynamic cavitation flow (PW-HCF), the Zwart-Gerber-Belamri (ZGB) cavitation model (Zwart et al., 2004) was employed. This model is derived from a reduced form of the Rayleigh-Plesset equation. The evaporation and condensation source terms are defined as follows:

$$R_e = F_{vap}\frac{3\rho_v(1 - \alpha_v)\alpha_{nuc}}{r_b}\sqrt{\frac{2}{3}\frac{p_v - p}{\rho_l}} \quad (p \le p_v) \tag{21}$$

$$R_c = F_{cond}\frac{3\rho_v\alpha_v}{r_b}\sqrt{\frac{2}{3}\frac{p - p_v}{\rho_l}} \quad (p \ge p_v) \tag{22}$$

where α_{nuc} denotes the nucleation site volume fraction,

set at 5×10^{-4}; p_v denotes the saturated vapor pressure for pure water; r_b denotes the cavitation bubble radius. F_{vap} and F_{cond} are constants, with values of 50 and 0.01, respectively.

2.3.2 Solid Particle-Pure Water-Hydrodynamic Cavitation Flow

In the case of solid particle-pure water-hydrodynamic cavitation flow (SP-PW-HCF), the saturated vapor pressure is influenced by the presence of solid particles. This effect was measured experimentally under various concentration conditions at a working temperature of 25°C. A fitting relationship between the vapor pressure and solid particle concentration was established as depicted by Eq. (23) and Fig. 3.

$$P_{s-v}(\alpha_k) = 3\times10^6\alpha_k^2 - 3.5164\times10^4\alpha_k + 3722 \tag{23}$$

where P_{s-v} represents the saturated vapor pressure for SP-PW-HCF, α_k denotes the general form of solid particle concentration with k as a subscript with values 1, 2, and 3.

In Eqs. (21) and (22), P_v was substituted by P_{s-v}. The relationships between the evaporation and condensation source terms and the concentration were directly derived, as shown in the following equations:

$$R_{s-e} = F_{vap}\frac{3\rho_v(1 - \alpha_v)\alpha_{nuc}}{r_b}\sqrt{\frac{2}{3}\frac{(3\times10^6\alpha_s^2 - 3.5164\times10^4\alpha_s + 3722) - p}{\rho_l}} \quad (p \le p_{s-v}) \tag{24}$$

$$R_{s-c} = F_{cond}\frac{3\rho_v\alpha_v}{r_b}\sqrt{\frac{2}{3}\frac{p - (3\times10^6\alpha_s^2 - 3.5164\times10^4\alpha_s + 3722)}{\rho_l}} \quad (p \ge p_{s-v}) \tag{25}$$

where R_{s-e} and R_{s-c} denote the evaporation and condensation source terms for SP-PW-HCF, respectively.

3. NUMERICAL SIMULATION SETUP

3.1 Physical Model

The numerical simulations for PW-HCF and SP-PW-HCF were conducted using a two-dimensional nozzle, as depicted in Fig. 4. The nozzle dimensions were consistent with the physical model described by Nurick (1976).
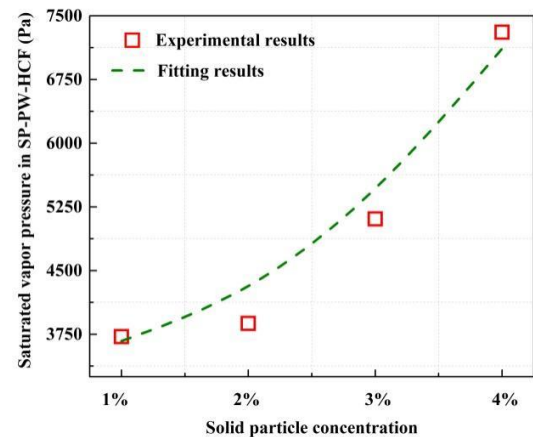

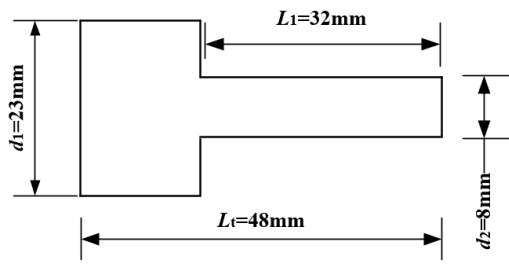**Fig. 3 Variation law of saturated vapor pressure in SP-PW-HCF**

Fig. 4 Two-dimensional nozzle

The total length of the nozzle is $L_t = 48$ mm, with an orifice length of $L_1 = 32$ mm. The inlet diameter is $d_1 = 23$ mm, and the outlet diameter is $d_2 = 8$ mm.

3.2 Mesh Generation

Discretization of the computational domain was performed using ANSYS-ICEM, employing quadrilateral meshes.

Previous theoretical analysis has demonstrated that the entire cavitation evolution process predominantly occurred within the orifice. To accurately capture the characteristics of PW-HCF and SP-PW-HCF, mesh refinement was applied in this region, as illustrated in Fig. 5. The total number of mesh elements was 55,346.

Mesh quality was assessed using the Determinant 3 × 3 × 3 feature in ANSYS-ICEM, with a value exceeding 0.95, satisfying the simulation requirements.

Mesh independence was evaluated using seven different mesh sets, as detailed in Table 1. The number of meshes ranged from 17,744 to 70,979 and was categorized as Coarse-A, Coarse-B, Medium-C, Medium-D, Medium-E, Fine-F, and Fine-G.

The nozzle discharge coefficient, C_d, was defined and used to assess mesh independence for PW-HCF and SP-PW-HCF.
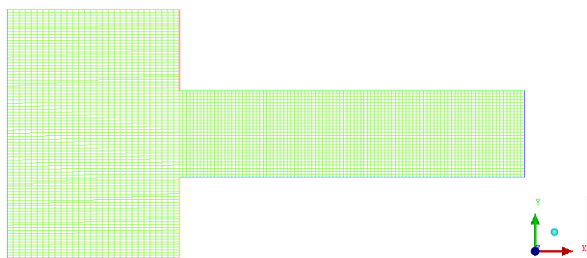
Fig. 5 Mesh of the computational domain

Table 1 Total mesh number

Name	Number
Coarse-A	17,744
Coarse-B	26,104
Medium-C	34,644
Medium-D	46,166
Medium-E	55,346
Fine-F	63,258
Fine-G	70,979

Because PW-HCF and SP-PW-HCF are different types of multiphase flows, their expressions for C_d demonstrate some differences. For PW-HCF, C_d was substituted by C_{wd} and is expressed as follows:

$$C_{wd} = \frac{m}{L\sqrt{2\rho_1(P_1 - P_2)}} \tag{26}$$

For SP-PW-HCF, it was denoted as C_{sd} and expressed as follows:

$$C_{sd} = \frac{m}{L\sqrt{2\rho_{m-w-s}(P_1 - P_2)}} \tag{27}$$

where m denotes the mass flow rate, L denotes the length of outlet edge, P_1 and P_2 represent the inlet and outlet total pressures, respectively, and ρ_{m-w-s} is the mixture density of water and solid particles, calculated as follows:

$$\rho_{m-w-s} = \rho_1\alpha_1 + \rho_s\alpha_s \tag{28}$$

Mesh independence assessments for PW-HCF and SP-PW-HCF were conducted with $d_s = 0.0055$ mm and $\alpha_s = 3\%$. The results are shown in Fig. 6.

The values of C_{wd} and C_{sd} exhibited a sharp decrease from Coarse-A to Medium-C, with minimal differences from Medium-C to Fine-G.

For PW-HCF, the maximum relative error was less than 0.073%, and for SP-PW-HCF, the error was less than 0.018%.
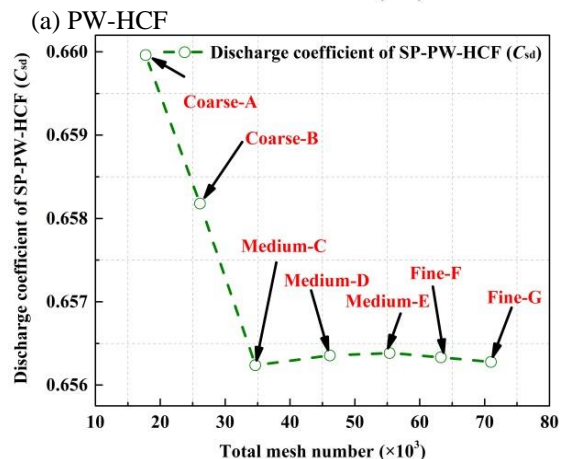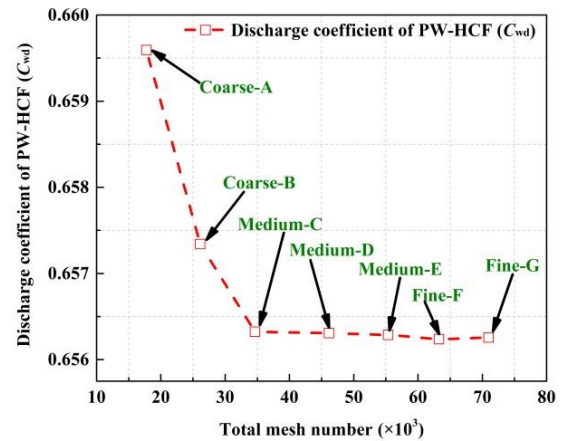
(a) PW-HCF

(b) SP-PW-HCF ($d_s = 0.0055$mm and $\alpha_s = 3\%$)
Fig. 6 Mesh independence assessment

Based on these results, Medium-E with 55,346 meshes was selected for the numerical simulations of PW-HCF and SP-PW-HCF.

4. VALIDATION AND VERIFICATION OF THE NUMERICAL ALGORITHM

4.1 Pure Water-Hydrodynamic Cavitation Flow

The numerical simulation of PW-HCF was conducted with $P_1 = 2.5 \times 10^8$ Pa and $P_2 = 9.5 \times 10^4$ Pa in the nozzle. The numerical results were compared with data from the ANSYS Fluid Dynamics Verification Manual (ANSYS, Inc., 2013).
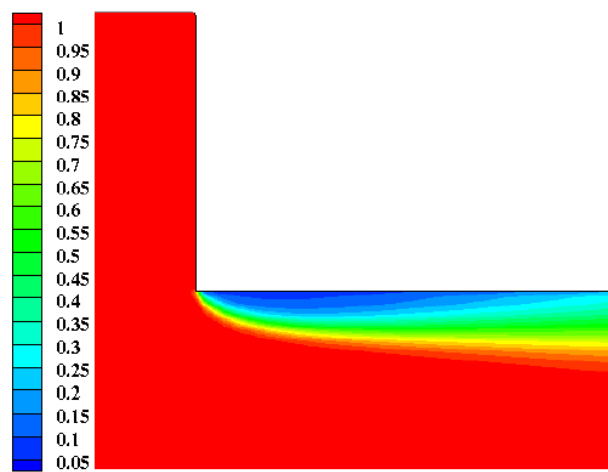
The water volume fraction near the orifice boundary was low, whereas it was significantly higher in other regions. The numerical results closely matched the literature data, as shown in Fig. 7. This agreement indicates that the algorithm used for simulating PW-HCF was validated effectively.
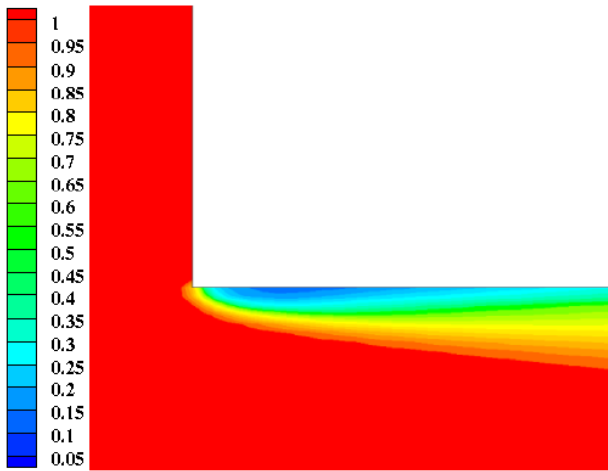
(a) Literature result

(b) Numerical result

Fig. 7 Comparison of water volume fraction distribution
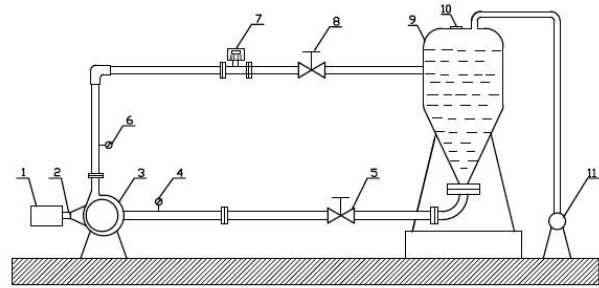
Notes: 1. Motor; 2. Torque and speed sensor; 3. Model centrifugal pump; 4. Inlet pressure transducer; 5. Water brake valve; 6. Outlet pressure transducer; 7. Flow meter; 8. Control valve; 9. Water tank; 10. Entrance of solid particles; 11. Vacuum pump

Fig. 8 Sketch of the rig

4.2 Solid Particle-Pure Water-Hydrodynamic Cavitation Flow

Experiments involving SP-PW-HCF were previously conducted in a centrifugal pump. Numerical simulations were also performed and compared with the experimental results to evaluate the suitability of the algorithm.

The closed experimental rig, depicted in Fig. 8, was used for SP-PW-HCF experiments in a centrifugal pump with $d_s = 0.5$ mm and $\alpha_s = 3\%$, under various pressure conditions at high flow rates.

The centrifugal pump was the primary equipment in the rig. Its performance parameters were: designed flow rate $Q_d = 25$ m³/h, designed head $H_d = 32$ m, efficiency $\eta = 52\%$, and specific speed $n_s = 34$.

The main device parameters include the motor, which is of type Y2-132M-4 with a rated power of 7.5 kW, rated voltage of 380 V, rated current of 15.6 A, rated rotational speed of 1440 rpm, and rated efficiency of 87%. The pressure transducer used is of type AXY-110/C, with a measurement range of 0-0.7 MPa and an accuracy grade of 0.5 FS. The flow meter, type AQU-50-1, has a measurement range of 4-40 m³/h and an accuracy grade of 0.5 FS. The torque and speed sensor, type JC1, is rated for a torque of 50 N·m, operates within a rotational speed range of 0-8000 rpm, and has an accuracy grade of 0.5 FS.

An innovative water tank, featuring an inverted conical bottom, was employed to ensure effective mixing of water and solid particles. This design significantly reduces automatic settling of solid particles and performs similarly to a virtual stirring device.

For the SP-PW-HCF experiments, solid particles with specific diameters were required. To obtain particles with the appropriate diameters, a top hammer type standard oscillating screen was utilized for separation. The screen's main performance parameters are as follows: type XSB-88/Φ = 200 mm, screen frame height 400 mm, radius of gyration 12.5 mm, gyration frequency 221 times/min, and oscillation frequency 147 times/min.

The flow rate through the model centrifugal pump is measured using Flow Meter 7. The centrifugal pump inlet velocity v_1 is calculated using the following equation.

$$v_1 = \frac{Q}{A_1} \qquad (29)$$

where Q denotes the volume flow rate, and A_1 denotes the inlet cross-section of the centrifugal pump.

Cavitation evolution is assessed using the net positive suction head (*NPSH*) in fluid machinery. The formula for *NPSH* is given by Eq. (30).

$$NPSH = \frac{P_{abs1}}{\rho_1 g} + \frac{v_1^2}{2g} - \frac{P_v}{\rho_1 g} \qquad (30)$$

where P_{abs1} denotes the inlet absolute pressure of the centrifugal pump.

Inlet and outlet total pressures, P_{in} and P_{out}, were measured using transducers 4 and 6. For PW-HCF, the head is calculated using Eq. (31).

$$H = \frac{P_{out} - P_{in}}{\rho_1 g} \qquad (31)$$

To calculate the net positive suction head and head for SP-PW-HCF, Eqs. (30) and (31) were modified. ρ_l was substituted by $\rho_{m\text{-}w\text{-}s}$ to account for the effects of solid particles, and P_v was substituted with $P_{s\text{-}v}$. The revised formulas are as follows:

$$NPSH_{SP} = \frac{P_{s\text{-}abs1}}{\rho_{m\text{-}w\text{-}s} g} + \frac{v_{s\text{-}1}^2}{2g} - \frac{P_{s\text{-}v}}{\rho_{m\text{-}w\text{-}s} g} \qquad (32)$$

$$NPSH_{SP} = \frac{P_{s\text{-}abs1}}{\rho_{m\text{-}w\text{-}s} g} + \frac{v_{s\text{-}1}^2}{2g} - \frac{3 \times 10^6 \alpha_k^2 - 3.5164 \times 10^4 \alpha_k + 3722}{\rho_{m\text{-}w\text{-}s} g} \qquad (33)$$

$$H_{SP} = \frac{P_{s\text{-}out} - P_{s\text{-}in}}{\rho_{m\text{-}w\text{-}s} g} \qquad (34)$$

where $NPSH_{SP}$ represents the net positive suction head for SP-PW-HCF, and H_{SP} represents the head. $P_{s\text{-}in}$ and $P_{s\text{-}out}$ are the total inlet and outlet pressures for SP-PW-HCF, respectively. $P_{s\text{-}abs1}$ denotes the absolute pressure, and $v_{s\text{-}1}$ denotes the inlet velocity of the centrifugal pump for SP-PW-HCF.

Using these methods, experimental values for $NPSH_{SP}$ and H_{SP} were calculated, and the performance curve was generated.

The SP-PW-HCF in the centrifugal pump was simulated using the fundamental equations from Section 2.1, along with the turbulence model from Section 2.2 and the cavitation model from Section 2.3.2. The resulting numerical performance curve is shown in Fig. 9.

Under high-pressure conditions, $NPSH_{SP}$ was substantial, indicating a non-cavitating state. The differences in H_{SP} were minimal. As pressure decreased steadily, $NPSH_{SP}$ decreased, leading to increased cavitation and a noticeable decrease in H_{SP}.
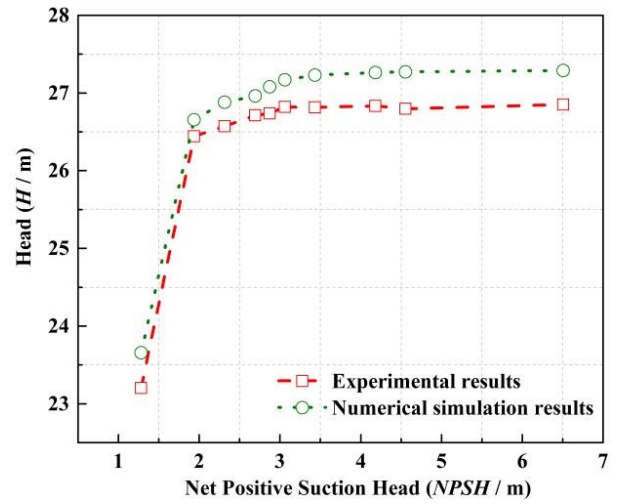

Fig. 9 Experimental and numerical SP-PW-HCF cavitation performance curves

(a) Experimental result
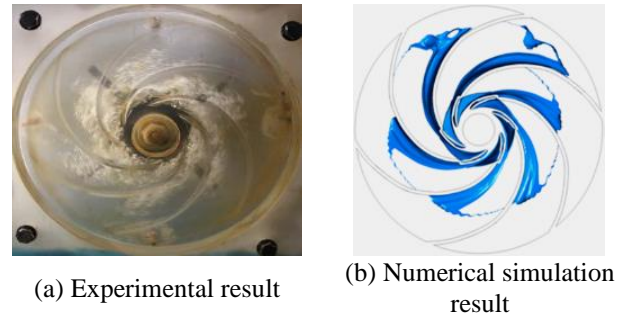
(b) Numerical simulation result

Fig. 10 Distribution of vapor in the impeller with $NPSH_{sp} = 2.693$ m

The maximum relative error was less than 1.95%, with numerical results aligning closely with experimental data.

Notably, the experimental results were lower than the numerical simulations because of losses from wear-ring clearance leakage.

Additionally, the distribution of vapor in the impeller with $NPSH_{sp} = 2.693$ m was compared between experimental and numerical results, as shown in Fig. 10. The numerical simulation results were consistent with the experimental observations.

5. RESULTS AND DISCUSSION

5.1 Distribution of Pressure, Vapor, Water, and Solid Particles

The distribution of pressure, water, vapor, and solid particles was analyzed using a case of SP-PW-HCF with $d_s = 0.0055$ mm and $\alpha_s = 2\%$. The distributions were symmetrical across the nozzle. In this numerical simulation, the inlet pressure was $P_1 = 2.5 \times 10^8$ Pa, and the outlet pressure was $P_2 = 9.5 \times 10^4$ Pa. The calculation residual was 10^{-8}.

Figure 11 illustrates the pressure distribution, with high pressure observed at the initial part of the nozzle
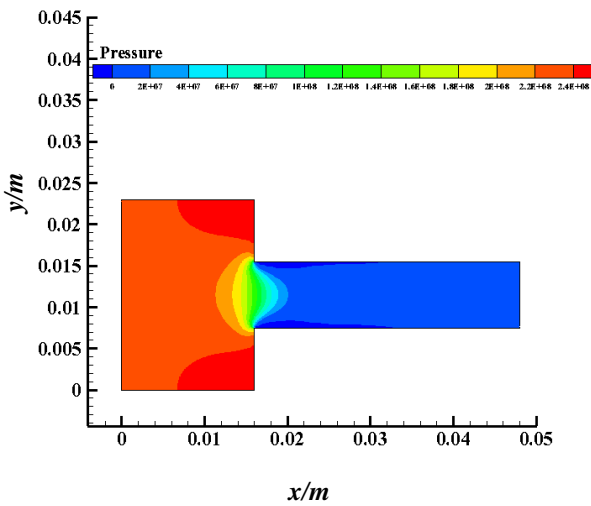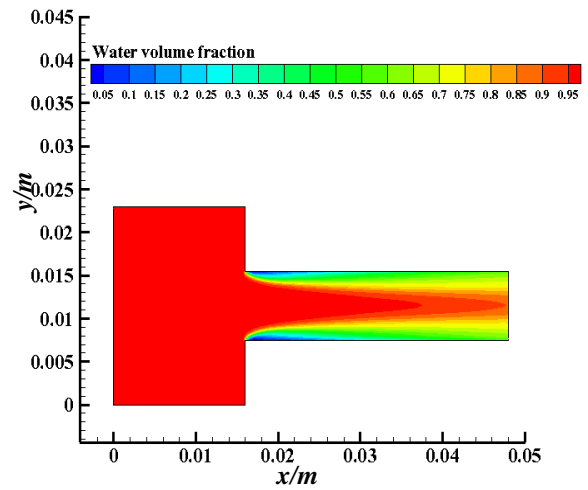
Fig. 11 Distribution of pressure

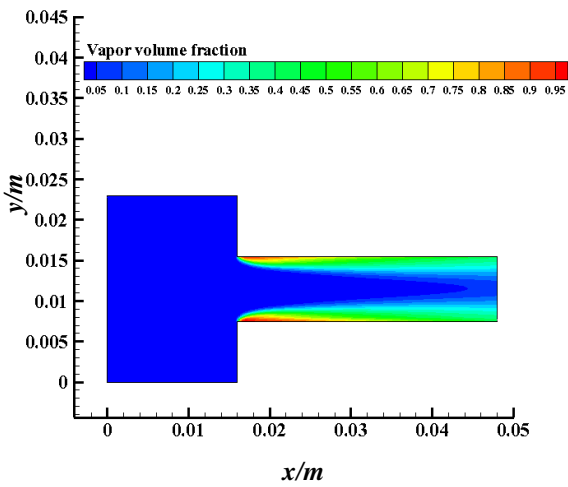**Fig. 13 Distribution of water volume fraction**

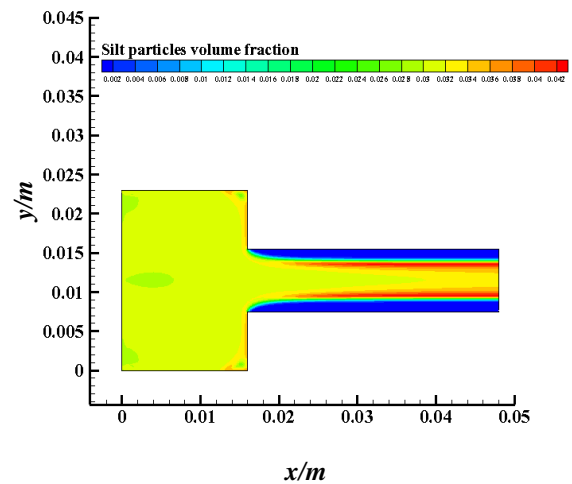**Fig. 12 Distribution of vapor**

Fig. 14 Distribution of solid particle volume fraction

and low pressure in the orifice. The minimum pressure occurred on both sides of the orifice, corresponding to the vapor volume fraction distribution shown in Fig. 12. The phase change between water and vapor resulted in a distribution of water volume fraction that was the inverse of the vapor distribution, as depicted in Fig. 13. Solid particles with high volume fractions were distributed around regions with high vapor volume fractions, as shown in Fig. 14, indicating a significant impact of solid particles on the evolution of SP-PW-HCF. In Figs. 11 through 14, the horizontal coordinate represents the nozzle length, and the vertical coordinate represents the nozzle diameter. This interpretation applies to all subsequent figures as well.

5.2 Cavitation Flow Evolution Process

The evolution of SP-PW-HCF with $d_s = 0.0055$ mm and $\alpha_s = 5\%$ was also examined. The complete evolution from $t_1 = 7.25 \times 10^{-8}$ s to $t_{14} = 2.975 \times 10^{-7}$ s is illustrated in Fig. 15, indicating a periodic variation.

Cavitation bubbles initially appeared at the beginning of the orifice, where the local pressure was below the saturated vapor pressure, with a bubble fraction of 5.42×10^{-4}.

As the pressure decreased from $t_1 = 7.25 \times 10^{-8}$ s to $t_2 = 9.75 \times 10^{-8}$ s, the bubbles grew in size, and the fraction increased.

As the pressure continued to decrease, the length and thickness of the bubbles increased steadily from $t_2 = 9.75 \times 10^{-8}$ s to $t_4 = 1.475 \times 10^{-7}$ s, with the evolution moving toward the outlet. The bubble fraction showed a significant increase.

At $t_5 = 1.600 \times 10^{-7}$ s, the bubble length was approximately half the length of the orifice. By $t_6 = 1.725 \times 10^{-7}$ s, the bubble length reached two-thirds of the orifice length, and by $t_7 = 1.850 \times 10^{-7}$ s, it extended to four-fifths of the length. Concurrently, the bubble fraction increased, indicating substantial cavitation development. At $t_8 = 1.975 \times 10^{-7}$ s, the bubbles reached the outlet and the fraction peaked.
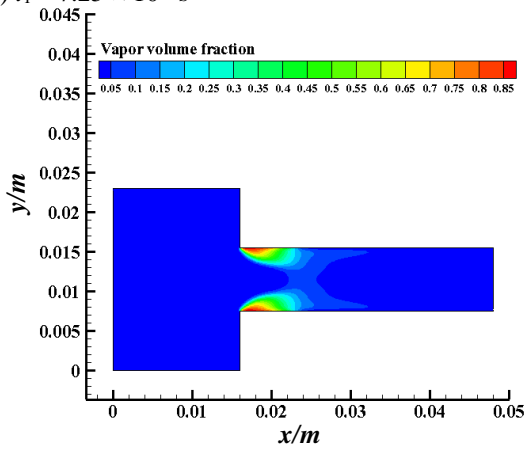
From $t_8 = 1.975 \times 10^{-7}$ s to $t_{14} = 2.975 \times 10^{-7}$ s, the bubble length gradually decreased and the fraction diminished. By the final time point, the bubbles and fraction returned to their initial states.
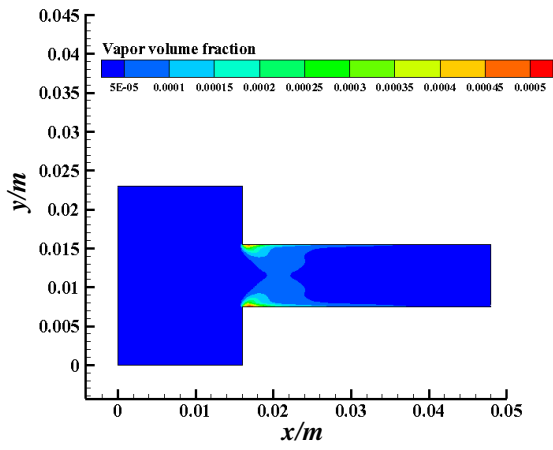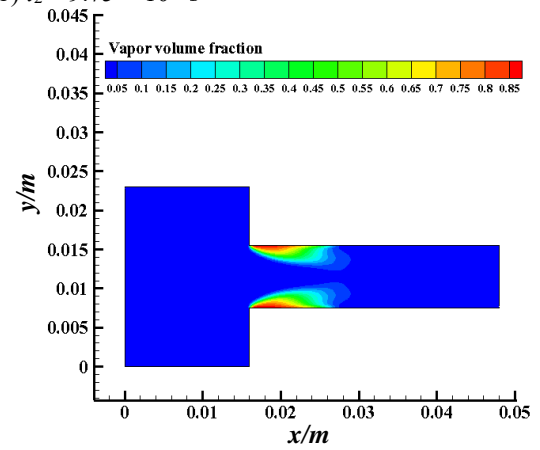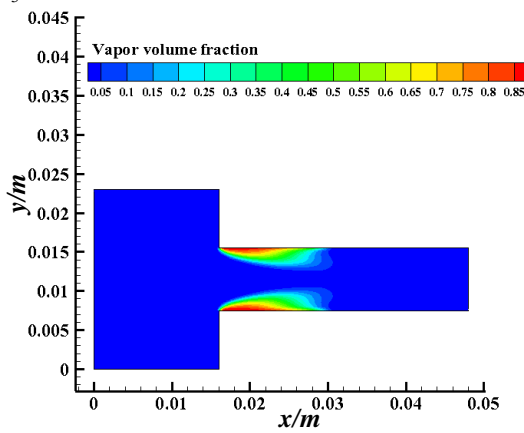
(a) $t_1 = 7.25 \times 10^{-8}$ s
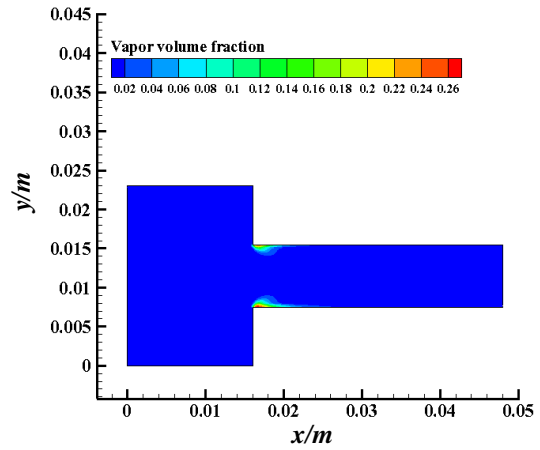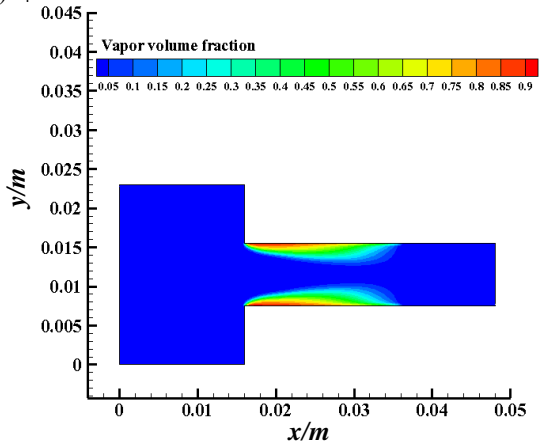
(b) $t_2 = 9.75 \times 10^{-8}$ s
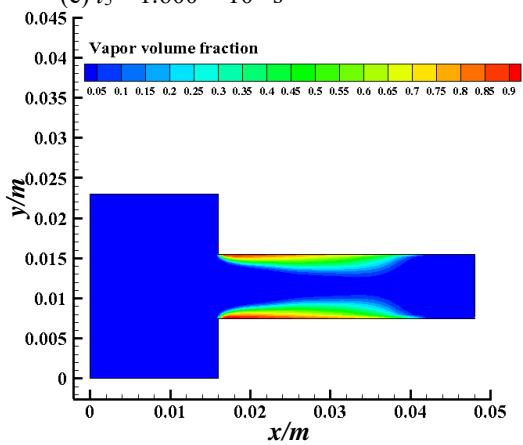
(c) $t_3 = 1.225 \times 10^{-7}$ s

(d) $t_4 = 1.475 \times 10^{-7}$ s
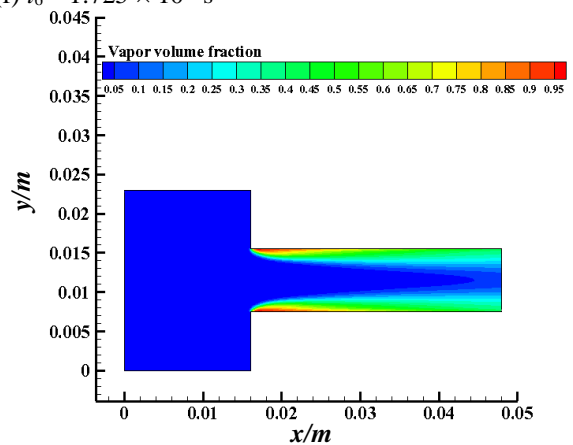
(e) $t_5 = 1.600 \times 10^{-7}$ s

(f) $t_6 = 1.725 \times 10^{-7}$ s

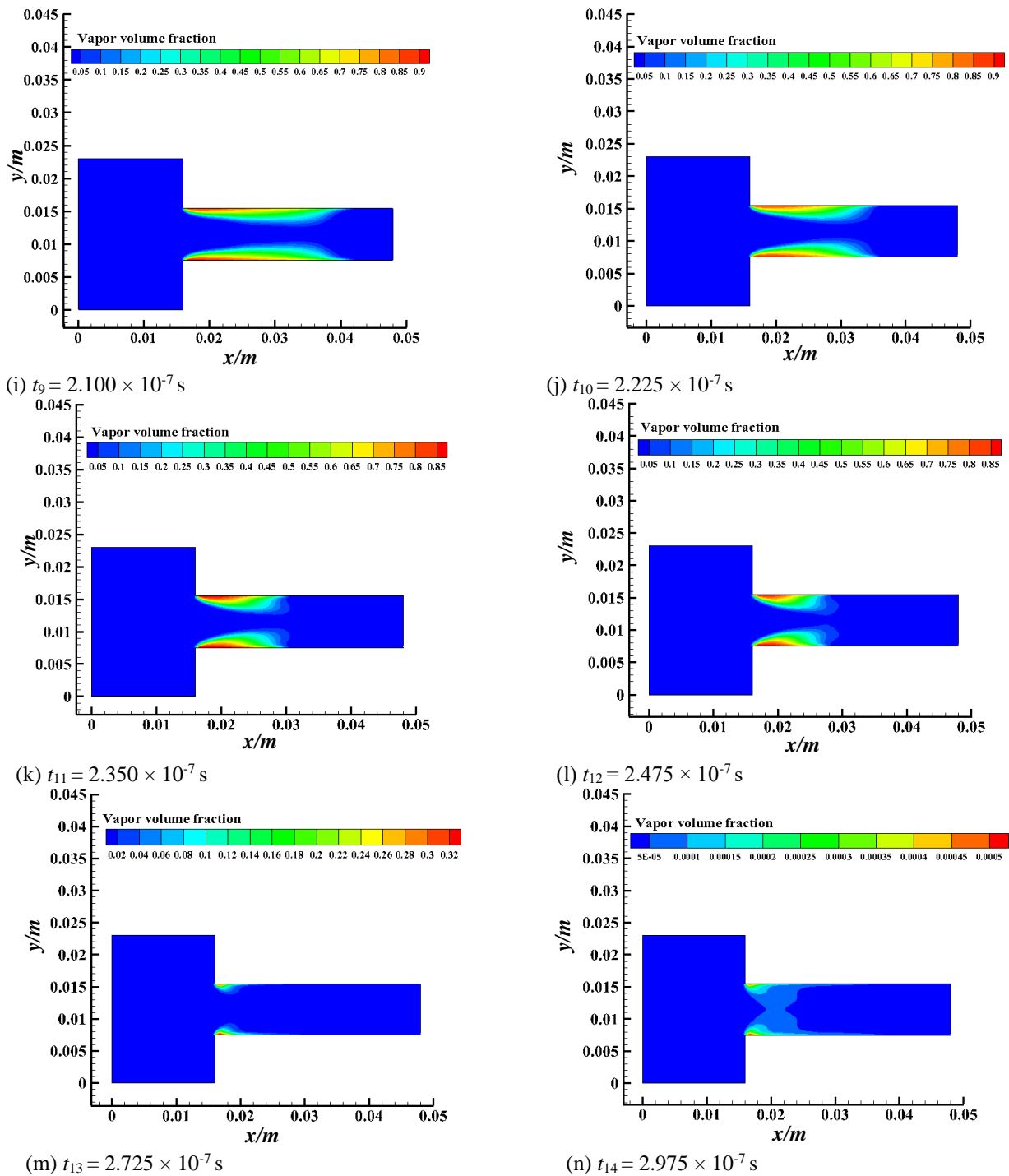(g) $t_7 = 1.850 \times 10^{-7}$ s

(h) $t_8 = 1.975 \times 10^{-7}$ s

(i) $t_9 = 2.100 \times 10^{-7}$ s

(j) $t_{10} = 2.225 \times 10^{-7}$ s

(k) $t_{11} = 2.350 \times 10^{-7}$ s

(l) $t_{12} = 2.475 \times 10^{-7}$ s

(m) $t_{13} = 2.725 \times 10^{-7}$ s

(n) $t_{14} = 2.975 \times 10^{-7}$ s

Fig. 15 Cavitation flow evolution process

5.3 Variation Laws of Vapor Content

Figure 16 presents the variations in vapor content for SP-PW-HCF at concentrations ranging from $\alpha_s = 5\%$ to 10%, collected over one cycle.

For $\alpha_s = 5\%$ and 6%, the mean diameter increased from 0.0015 mm to 0.040 mm. A consistent observation was that all vapor contents for SP-PW-HCF were higher than those for PW-HCF, indicating that solid particles promoted SP-PW-HCF evolution.

The variation patterns exhibited both similarities and differences. The similarities included a gradual decrease in vapor content with increasing mean diameter from 0.0015 mm to 0.0095 mm. However, when the diameter increased from 0.0095 mm to 0.015 mm, the decrease was particularly sharp.

The differences emerged between diameters of 0.015 mm to 0.040 mm. At $\alpha_s = 5\%$, the vapor content initially decreased and then increased. Conversely, for $\alpha_s = 6\%$, the content increased slightly, then decreased, and increased again at larger diameters.

At $\alpha_s = 6\%$, the vapor content for diameters between 0.0015 mm and 0.0075 mm was slightly higher than at $\alpha_s = 5\%$, indicating a marginally stronger promotion effect.

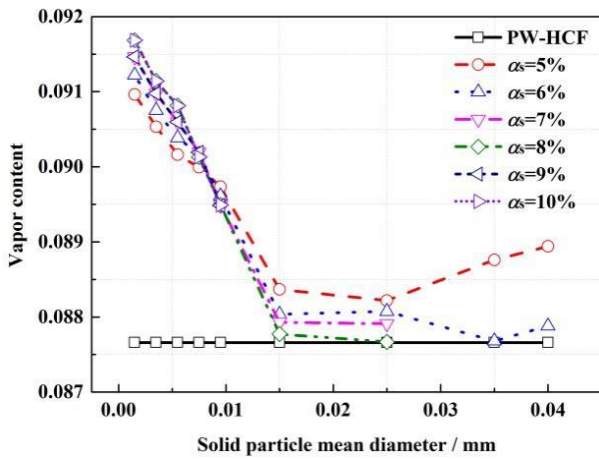However, for diameters from 0.0095 mm to 0.040

Fig. 16 Variations in vapor content

mm, the trend was opposite, with $\alpha_s = 6\%$ showing slightly lower contents compared to $\alpha_s = 5\%$, and weaker promotion.

For $d_s = 0.035$ mm and 0.040 mm, the vapor content at $\alpha_s = 5\%$ was considerably higher than at $\alpha_s = 6\%$, demonstrating much stronger stimulation effects at $\alpha_s = 5\%$.

At $\alpha_s = 6\%$, the vapor contents for $d_s = 0.035$ mm and 0.040 mm were slightly higher than in PW-HCF, with relative differences of 0.023% and 0.25%, respectively, indicating a modestly stronger stimulation than in PW-HCF.

At $\alpha_s = 7\%$ and 8%, vapor contents for diameters from 0.0015 mm to 0.025 mm were higher than in PW-HCF. Solid particles thus contributed to cavitation flow evolution.

The variation laws for $\alpha_s = 7\%$ and 8% were almost identical. For diameters from 0.0015 mm to 0.0095 mm, vapor content decreased gradually, leading to a steady weakening of the promotion effect.

For $d_s = 0.0095$ mm to 0.015 mm, vapor content decreased sharply, and the promotion strength significantly diminished. For diameters from 0.015 mm to 0.025 mm, the vapor content decreased slightly, with a correspondingly slight weakening of the stimulation effect.

When comparing $\alpha_s = 8\%$ with $\alpha_s = 7\%$, the vapor content for diameters from 0.0015 mm to 0.0095 mm was slightly higher for $\alpha_s = 8\%$, indicating marginally stronger promotion.

For $d_s = 0.015$ mm and 0.025 mm, the trends reversed, with $\alpha_s = 7\%$ exhibiting slightly higher contents and more intense stimulation compared to $\alpha_s = 8\%$.

At $d_s = 0.015$ mm and 0.025 mm, the vapor contents for $\alpha_s = 7\%$ and 8% were slightly higher than in PW-HCF, with a minimal increase in promotion degree compared to SP-PW-HCF with $\alpha_s = 5\%$ to 6%.

For $\alpha_s = 9\%$ and 10%, SP-PW-HCF with diameters from 0.0015 mm to 0.0095 mm exhibited higher vapor contents than in PW-HCF, indicating that solid particles

continued to promote cavitation flow development.

For $\alpha_s = 9\%$ and 10%, the common trend was a consistent decrease in vapor content with increasing mean diameter, accompanied by a steady reduction in stimulation strength and minimal differences.

At $d_s = 0.0015$ mm and 0.0035 mm, vapor contents for $\alpha_s = 10\%$ were noticeably higher than for $\alpha_s = 9\%$, with more intense promotion effects.

For $d_s = 0.0055$ mm and 0.0075 mm, the vapor contents were slightly higher than at $\alpha_s = 9\%$, with slightly stronger stimulation intensities. However, for $d_s = 0.0095$ mm, the vapor content for $\alpha_s = 10\%$ was lower than for $\alpha_s = 9\%$, demonstrating weaker promotion intensity.

Overall, the variation laws were consistent with those observed for SP-PW-HCF with $\alpha_s = 5\%$ to 6% and 7% to 8%, with the most noticeable difference being that all vapor contents were considerably higher compared to PW-HCF.

6. MECHANISM REVELATION

6.1 Cavitation Nuclei

The number of cavitation nuclei is a critical factor influencing cavitation flow development (Washio, 2014). In SP-PW-HCF, solid particles can induce a greater number of cavitation nuclei, thereby promoting cavitation evolution.

Figure 17 illustrates the variation process of cavitation nuclei on the surfaces of a single solid particle. First, cavitation nuclei form on the solid particle's surface. As pressure continuously decreases, these nuclei detach from the solid particle. With the steady reduction in pressure, the number of nuclei increases, and the size of the bubbles enlarges. Finally, the first large bubble detaches from the surface of the solid particle.
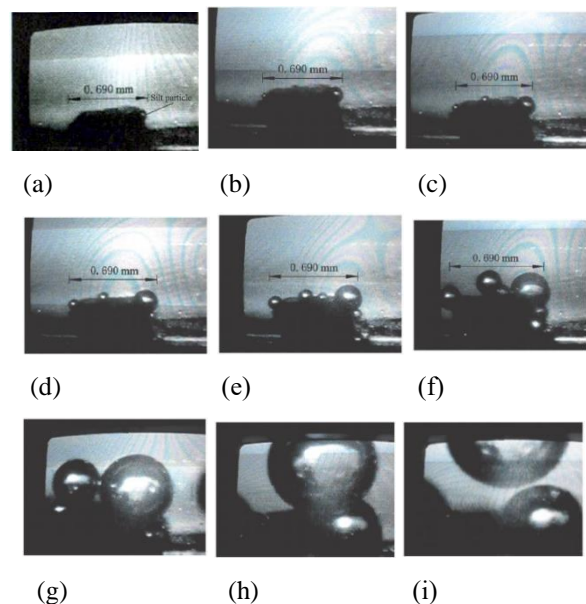

(a) (b) (c)

(d) (e) (f)

(g) (h) (i)

Fig. 17 Variation process of cavitation nuclei on the surface of a solid particle

495

(a) Vapor
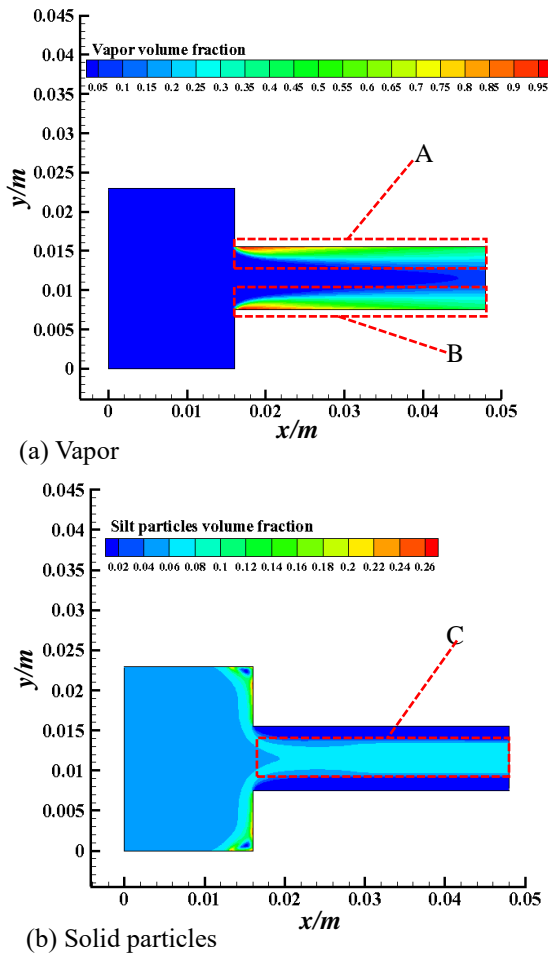
(b) Solid particles

Fig. 18 Distributions of vapor and solid particles in the nozzle

Fig. 19 Distribution of slip velocity in PW-HCF

For d_s = 0.0015 mm and α_s = 5%, it was analyzed to examine the distributions of vapor and solid particle volume fractions within the nozzle, as illustrated in Fig. 18.

In regions A and B, where the vapor volume fraction is high, the solid particle volume fraction is also elevated, as depicted in region C. The presence of solid particles results in the generation of additional cavitation nuclei, which enhances the evolution of SP-PW-HCF within the nozzle. These findings are corroborated by numerical simulation results.

6.2 Slip Velocity

6.2.1 Distribution of Slip Velocity

The distributions of slip velocity in PW-HCF and representative cases of SP-PW-HCF are illustrated in Figs. 19 and 20. Slip velocities between solid particles with water and between vapor with water were calculated. Then, the total one was got.

Slip velocity, which occurs between phases, shows symmetrical distributions in both PW-HCF and SP-PW-HCF. In regions with a high vapor volume fraction, slip velocity values are elevated, with SP-PW-HCF exhibiting higher values compared to PW-HCF. The presence of solid particles significantly influences these variations, affecting the development of SP-PW-HCF.
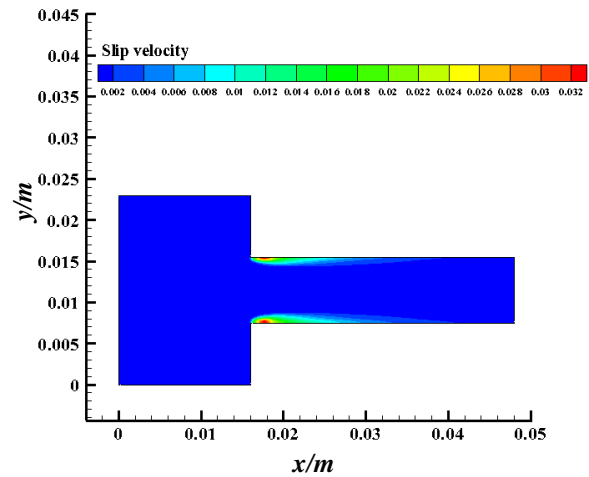
6.2.2 Variation Laws of Maximum and Minimum Values

Figure 21 illustrates the variations in maximum and minimum slip velocities in SP-PW-HCF across α_s values from 5% to 10%. The data were collected over one cycle.

For the maximum slip velocity, values were consistently higher than those observed in PW-HCF. The maximum slip velocity increased gradually with the mean diameter. When the mean diameter was at its smallest, the differences between the maximum slip velocities of SP-PW-HCF and PW-HCF were marginal.

The maximum slip velocities reached their peak at d_s = 0.040 mm, considerably exceeding those in PW-HCF. At α_s = 6%, the maximum slip velocities exceeded those at α_s = 5%. For diameters varying from 0.0015 mm to 0.015 mm, the differences between the maximum slip velocities for 5% with 6% were minimal, but these differences increased with diameter.

The minimum slip velocities decreased with increasing mean diameter and were consistently lower than those in PW-HCF, although the absolute values were still higher. The minimum slip velocities were lowest at d_s = 0.040 mm, with values for α_s = 5%, being higher than those for α_s = 6%.

Similar to the maximum slip velocities, the differences in minimum slip velocities were small from 0.0015 mm to 0.015 mm but became more pronounced from 0.025 mm to 0.040 mm.

At α_s = 7% and 8%, maximum slip velocities were higher than in PW-HCF. They increased gradually with mean diameter from 0.0015 mm to 0.025 mm, peaking at d_s = 0.025 mm. The maximum slip velocities at d_s = 0.0015 mm were slightly higher than those in PW-HCF. For other conditions, they were significantly higher than in PW-HCF, with values for α_s = 8% being higher than at α_s = 7%.

For d_s = 0.0015 mm to 0.0095 mm, the in maximum slip velocities were minimal, but differences increased steadily from 0.015 mm to 0.025 mm.
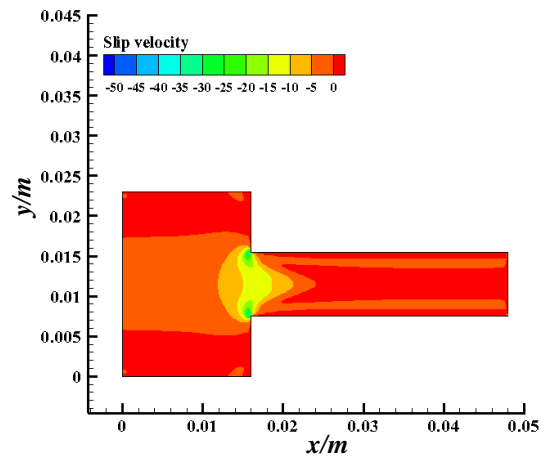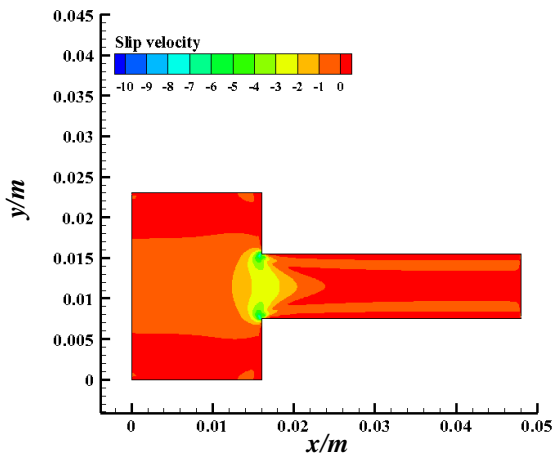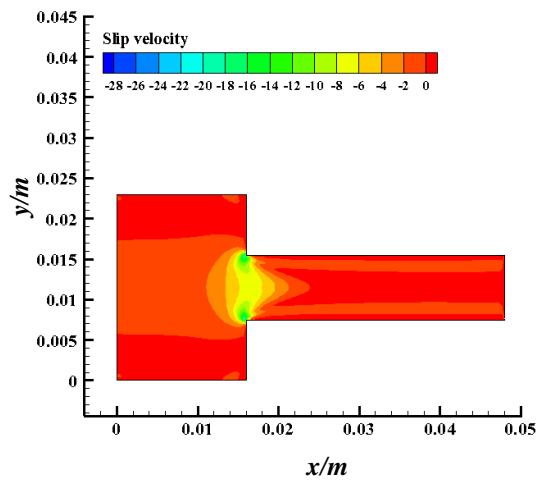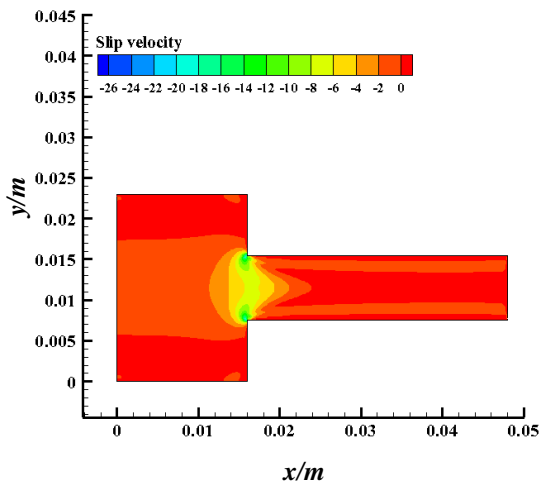
(a) d_s = 0.0055 mm and α_s = 5%

(b) d_s = 0.035 mm and α_s = 6%
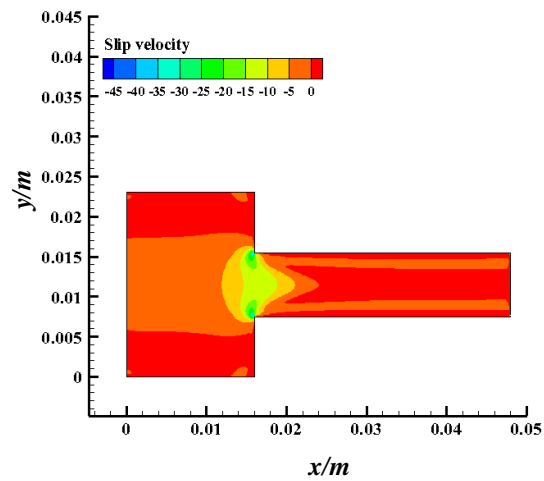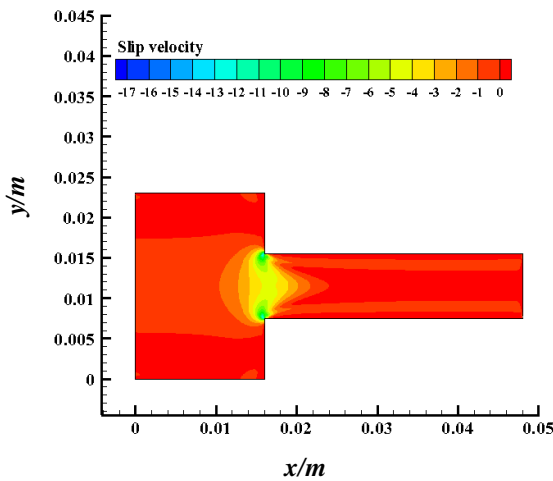
(c) d_s = 0.0075 mm and α_s = 7%

(d) d_s = 0.025 mm and α_s = 8%

(e) d_s = 0.0095 mm and α_s = 9%

(f) d_s = 0.0095 mm and α_s = 10%

**Fig. 20 Distribution of Slip Velocity in SP-PW-HCF**

The minimum slip velocities were lower than those in PW-HCF, with the values at d_s = 0.0015 mm being notably low. Peak and minimum values appeared at d_s = 0.0015 mm and 0.025 mm, respectively. For α_s = 7%, the values were higher than for α_s = 8%, with differences in minimum slip velocities being minimal from d_s = 0.0015 mm to 0.0095 mm but becoming more pronounced from d_s = 0.015 mm to 0.025 mm. For maximum slip velocities under α_s = 9% and 10%, values exceeded those in PW-HCF. They increased gradually with the mean diameter from 0.0015 mm to 0.0095 mm, peaking at d_s = 0.0095 mm. Values for α_s = 10% were slightly higher than for α_s = 9%, though the differences were minimal.

The minimum slip velocities were consistently lower
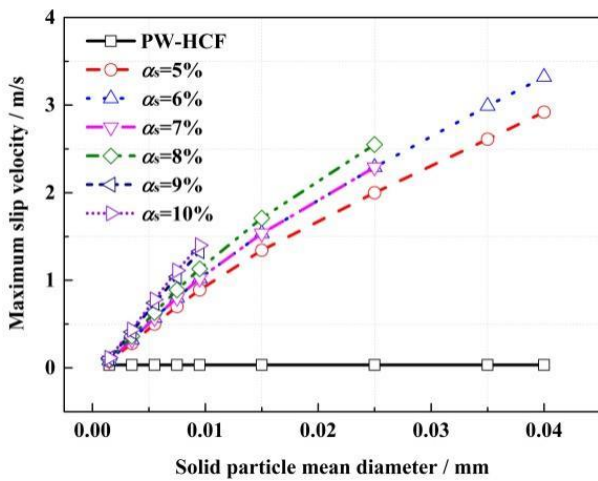
(a) Maximum slip velocity
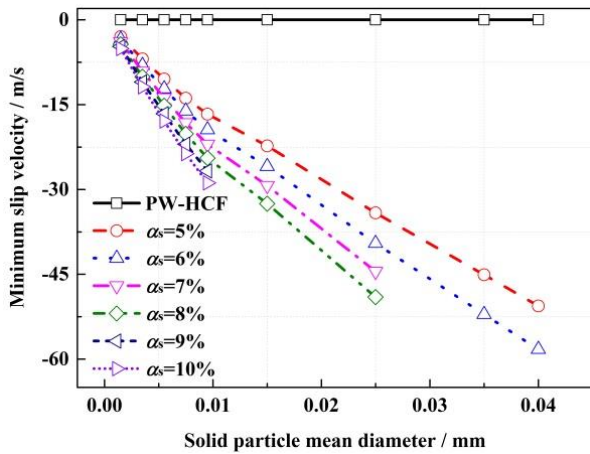
(b) Minimum slip velocity

Fig. 21 Variations of maximum and minimum slip velocities

Fig. 22 Distribution of turbulent kinetic energy in PW-HCF

than those in PW-HCF, decreasing steadily with diameter. The minimum slip velocities at d_s = 0.0095 mm were the lowest. At d_s = 0.0015 mm, minimum slip velocities were noticeably lower than in PW-HCF, with α_s = 9% exhibiting slightly higher values than α_s = 10%, though the differences were fractional.

Both the maximum and absolute minimum slip velocities were substantially higher than in PW-HCF. The reduction in pressure around solid particles contributed to the enhanced evolution of SP-PW-HCF within the nozzle (Zhao et al., 2017a, b).

Numerical simulation results aligned well with theoretical predictions, confirming slip velocity as a primary factor.

6.3 Turbulent Kinetic Energy

6.3.1 Distribution of Turbulent Kinetic Energy

The cases analyzed in this section are consistent with those in Section 6.2.1. The distributions of turbulent kinetic energy in PW-HCF and SP-PW-HCF are illustrated in Figs. 22 and 23.
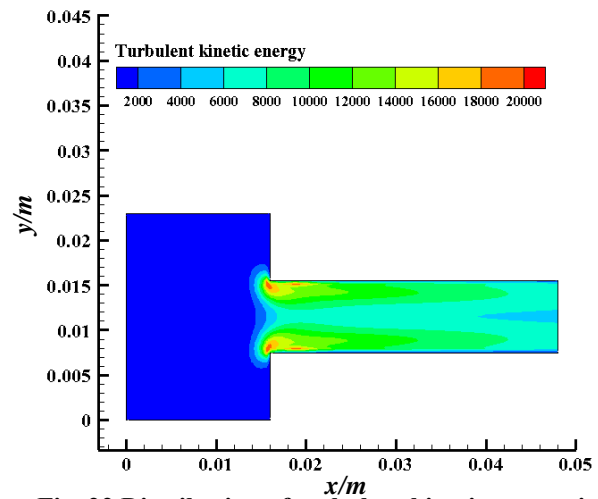
Both PW-HCF and SP-PW-HCF exhibit symmetrical

distributions of turbulent kinetic energy. High-intensity turbulent kinetic energy is observed in regions with a high vapor volume fraction, indicating a close relationship with cavitation evolution.

In SP-PW-HCF, the distribution region is larger, and the values are higher compared to PW-HCF.

6.3.2 Variation Laws of Maximum and Minimum Values

The variations in turbulent kinetic energy were analyzed using Tecplot software to obtain data on maximum and minimum values for one cycle.

Figure 24 compares these values in SP-PW-HCF with those in PW-HCF for α_s = 5% to 10%. Both maximum and minimum turbulent kinetic energies in SP-PW-HCF were consistently greater than those in PW-HCF.

For maximum turbulent kinetic energies, values decreased steadily with increasing mean diameter, showing a straightforward trend. Maximum turbulent kinetic energies were higher at α_s = 5% compared to α_s = 6%, and the difference between these percentages increased gradually.

The behavior of minimum turbulent kinetic energies was more complex. For α_s = 5% and 6%, the trend exhibited an initial decrease, followed by an increase, a subsequent decrease, and a final increase.

Notably, from 0.0035 mm to 0.0040 mm, the minimum turbulent kinetic energy increased slightly at α_s = 5% and decreased steadily at α_s = 6%. The peak value was observed at d_s = 0.025 mm, while the minimum values were d_s = 0.0095 mm for α_s = 5% and d_s = 0.0075 mm for α_s = 6%.

For maximum turbulent kinetic energies, the values in SP-PW-HCF were higher than those in PW-HCF and decreased with diameter, reaching a minimum at d_s = 0.025 mm. Values of α_s = 7% were higher than those for α_s = 8% with differences slightly increasing at d_s = 0.025 mm.

(a) $d_s = 0.0055$ mm and $\alpha_s = 5\%$

(b) $d_s = 0.035$ mm and $\alpha_s = 6\%$

(c) $d_s = 0.0075$ mm and $\alpha_s = 7\%$

(d) $d_s = 0.025$ mm and $\alpha_s = 8\%$

(e) $d_s = 0.0095$ mm and $\alpha_s = 9\%$

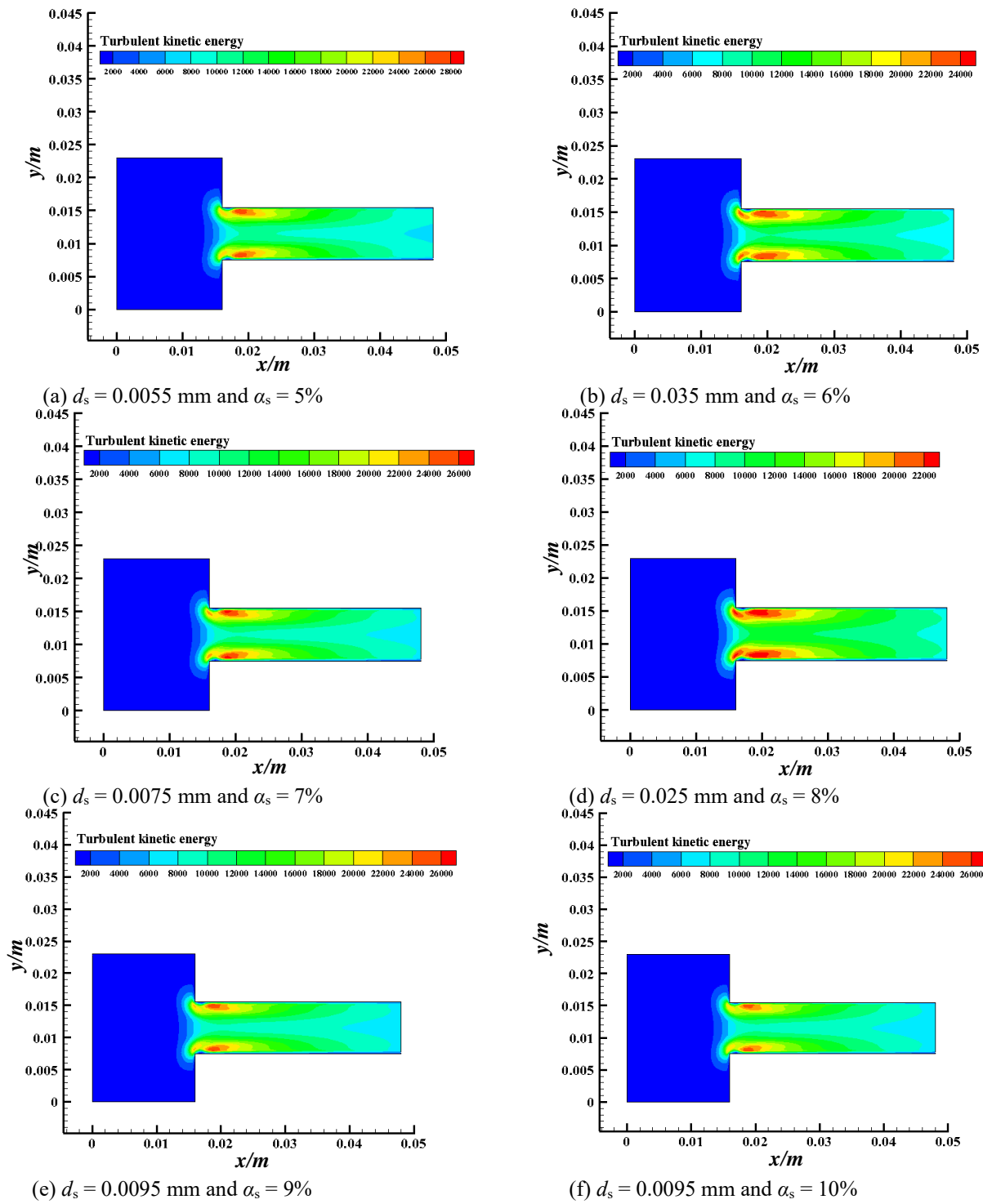(f) $d_s = 0.0095$ mm and $\alpha_s = 10\%$

**Fig. 23 Distribution of turbulent kinetic energy in SP-PW-HCF**

The minimum turbulent kinetic energies were also higher than in PW-HCF, initially decreasing before increasing. For $\alpha_s = 7\%$, the minimum value occurred at $d_s = 0.0075$ mm; for $\alpha_s = 8\%$, it occurred at 0.0035 mm. At $d_s = 0.0075$ mm and 0.0095 mm, the minimum turbulent kinetic energies for $\alpha_s = 8\%$ were higher than for $\alpha_s = 7\%$. For other conditions, the variations were reversed.

For maximum turbulent kinetic energy, trends similar to those observed at $\alpha_s = 7\%$ and 8% were evident. The maximum values consistently decreased with increasing diameter, reaching their lowest point at $d_s = 0.0095$ mm. Values for $\alpha_s = 9\%$ were higher than those

for $\alpha_s = 10\%$, with differences becoming slightly more pronounced.

Regarding minimum turbulent kinetic energy, all values exceeded those observed in PW-HCF. For $\alpha_s = 9\%$, values decreased from 0.0015 mm to 0.0035 mm, whereas for $\alpha_s = 10\%$, they increased.

As the mean diameter increased from 0.0025 mm to 0.0095 mm, the trend initially showed a decrease followed by an increase. At $d_s = 0.0075$ mm and 0.0095 mm, values for $\alpha_s = 10\%$ were higher than those for $\alpha_s = 9\%$. For other conditions, values were lower than those for $\alpha_s = 9\%$.
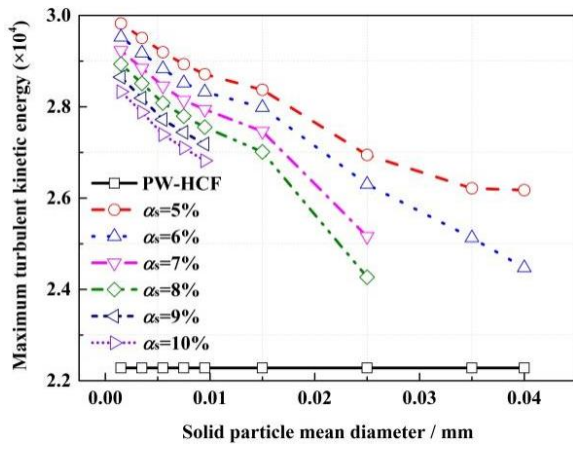
(a) Maximum turbulent kinetic energy
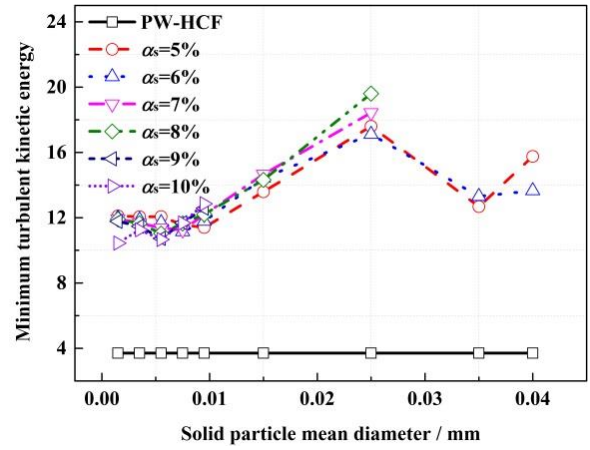
(b) Minimum turbulent kinetic energy

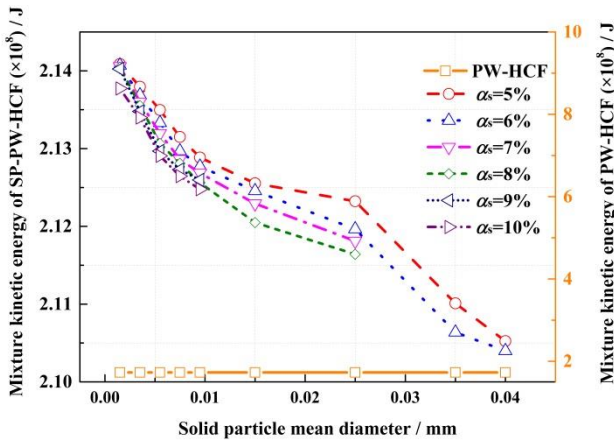**Fig. 24 Maximum and minimum turbulent kinetic energies**

Fig. 25 Variations of mixture kinetic energy

As discussed, the maximum and minimum turbulent kinetic energies in SP-PW-HCF were greater than those in PW-HCF. In SP-PW-HCF, the combined kinetic energies of water, vapor, and solid particles surpassed those of water and vapor alone in PW-HCF, as illustrated in Fig. 25. The pressure in SP-PW-HCF decreased significantly, with solid particles promoting the development of SP-PW-HCF. Turbulent kinetic energy emerged as a primary influencing factor.

6.4 Saffman Lift Force

6.4.1 Formula Modification

The Saffman lift force is a type of force that acts on solid particles (Saffman, 1965).

The general form of the Saffman lift force in SP-PWF is given by Eq. (35). In addition to the effects of the properties of solid particles and water, it is influenced by the water velocity gradient in the y-direction (first term) and the slip velocity between water and solid particles (second term), as shown in the following equation:

$$F_{L} = C_{LS} \frac{9.69}{\pi d_s \rho_s} \left(\rho_1 \mu_1 \right)^{1/2} \underbrace{\left| \frac{\partial u_1}{\partial y} \right|^{1/2}}_{No.1} \overset{No.2}{\overbrace{\left| u_1 - u_s \right|}} \tag{35}$$

where F_L denotes the general Saffman lift force, and C_{LS} is a coefficient.

In SP-PW-HCF, which contained both water and vapor, the formula was modified to account for the effects of the Saffman lift force on SP-PW-HCF evolution.

The modifications involved substituting ρ_1 and μ_1 in SP-PWF with mixture density of water and vapor $\rho_{m\text{-}w\text{-}v}$ in Eq. (36) and mixture viscosity $\mu_{m\text{-}w\text{-}v}$ in Eq. (37).

$$\rho_{m\text{-}w\text{-}v} = \rho_1 \alpha_1 + \rho_v \alpha_v \tag{36}$$

$$\mu_{m\text{-}w\text{-}v} = \mu_1 \alpha_1 + \mu_v \alpha_v \tag{37}$$

To fully incorporate the effects of vapor, the velocity gradient was added to the first term:

$$\frac{\partial u_1}{\partial y} + \frac{\partial u_v}{\partial y} \tag{38}$$

Slip velocity was then considered among water, vapor, and solid particles:

$$u_1 + u_v - u_s \tag{39}$$

The revised form is as follows:

$$F_{M\text{-}L} = C_{LS} \frac{9.69}{\pi d_s \rho_s} \left(\rho_{m\text{-}w\text{-}v} \mu_{m\text{-}w\text{-}v} \right)^{1/2} \underbrace{\left| \frac{\partial u_1}{\partial y} + \frac{\partial u_v}{\partial y} \right|^{1/2}}_{No.1} \overset{No.2}{\overbrace{\left| u_1 + u_v - u_s \right|}} \tag{40}$$

where $F_{M\text{-}L}$ denotes the modified Saffman lift force.

Theoretically, $F_{M\text{-}L}$ was greater than F_L. In PW-HCF, this force was nonexistent, and the pressure around solid particles decreased more significantly, thus promoting SP-PW-HCF development.

6.4.2 Distribution of Velocity Gradient of Water and Vapor in the Y Direction

The distribution characteristics of the water and vapor velocity gradient in the y-direction for SP-PW-HCF with $d_s = 0.0015$ mm and $\alpha_s = 1\%$ are depicted in Fig. 26.
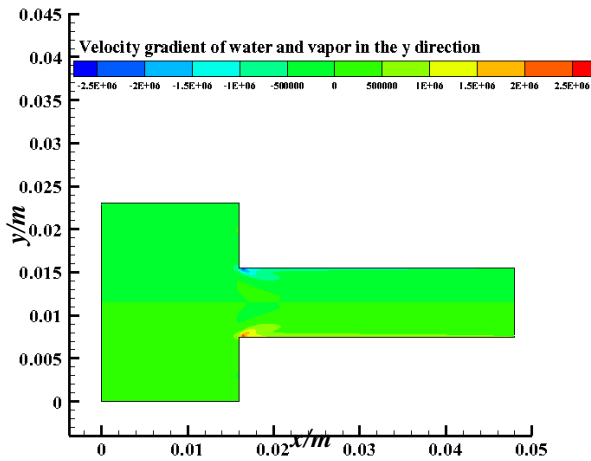
Fig. 26 Distribution of water and vapor velocity gradient in the *y* direction with d_s = 0.0015 mm and α_s = 1%
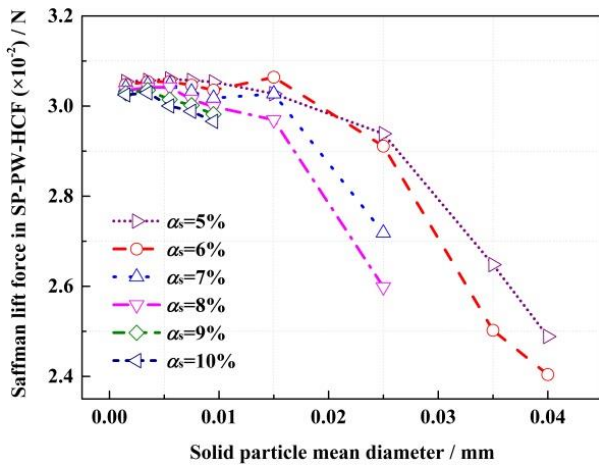

Fig. 27 Variations in Saffman lift force in SP-PW-HCF under all concentration conditions

The distribution of the velocity gradient in the *y* direction was asymmetrical, differing from the distributions of slip velocity and turbulent kinetic energy.

In regions with a high vapor volume fraction, variations in the gradient were substantial. Above the orifice, the values were negative, while below the orifice, they were positive. The variations in the velocity gradient were more complex.

6.4.3 Variations in Saffman Lift Force

Figure 27 illustrates the variations in Saffman lift force in SP-PW-HCF. For all concentration conditions, the magnitude of the force was relatively small, with values on the order of 10^{-2}.

Compared to slip velocity and turbulent kinetic energy, the impact of Saffman lift force on SP-PW-HCF was relatively weak, positioning it as a secondary factor.

7. CONCLUSIONS

Numerical simulations of PW-HCF and SP-PW-HCF were conducted in the nozzle, with concentration levels ranging from 5% to 10%. The vapor contents of SP-PW-HCF were compared with those of PW-HCF to assess the impact of solid particles. Variations in the properties of solid particles, flow fields, and forces acting on the particles were analyzed to elucidate the underlying mechanisms. The primary conclusions are as follows:

(1) Under all conditions, the vapor content in PW-HCF was lower than that in SP-PW-HCF. Solid particles contributed to the development of SP-PW-HCF, with the promoting effect diminishing as the concentration increased. The effective range of this promotion decreased from 0.0015 mm to 0.040 mm to between 0.0015 mm and 0.0095 mm as concentration increased from 5% to 10%.

(2) The number of cavitation nuclei in SP-PW-HCF exceeded that in PW-HCF, thereby promoting the development of SP-PW-HCF.

(3) Slip velocity and turbulent kinetic energy were the primary factors influencing the evolution of SP-PW-HCF.

(4) The magnitude of the Saffman lift force was on the order of 10^{-2}, indicating its role as a secondary factor in SP-PW-HCF development.

CONFLICT OF INTEREST

The authors declare no conflicts of interest

AUTHORS CONTRIBUTION

Dan Wang: Conceptualization, data curation, methodology, formal analysis, validation, writing-original draft, and writing-review & editing; **Weiguo Zhao**: Conceptualization, funding acquisition, investigation, methodology, supervision, and visualization; **Xiangdong Han**: Conceptualization, data curation, formal analysis, methodology, resources, validation, and visualization.

REFERENCES

ANSYS, Inc. (2013). *ANSYS fluid dynamics verification manual*. ANSYS, PA.

Bel Hadj Taher, A., Kanfoudi, H., & Zgolli, R. (2022). Numerical prediction approach of cavitation erosion based on 3d simulation flow. *Journal of Applied Fluid Mechanics*, *15*(4), 1165-1177. https://doi.org/10.47176/JAFM.15.04.1016

Chen, S. Y., Xu, W. L., Luo, J., Li, B. J., & Zhai, Y. W. (2021). Experimental study on the mesoscale causes of the effect of sediment size and concentration on material cavitation erosion in sandy water. *Wear*, *488-489*, 204114. https://doi.org/10.1016/j.wear.2021.204114

Chen, Y. W., Xia, B. Z., & Chen, B. (2015). Simulation on influence of blade structure and speed of classification wheel on classification performance. *China Powder Science and Technology*, *21*(4), 6-10. https://doi.org/10.13732/j.issn.1008-5548.2015.04.002

Das, S. K., & Chatterjee, D. (2023). *Vapor liquid two phase flow and phase change.* Springer. https://doi.org/10.1007/978-3-031-20924-6

Gidaspow, D., Bezburuah, R., & Ding, J. (1992). *Hydrodynamics of circulating fluidized beds, kinetic theory approach*. Proceedings of the 7th Engineering Foundation Conference on Fluidization, Brisbane.

Han, X. D., Kang, Y., Zhao, W. G., Sheng, J. P., & Li, D. (2019). Silt particles affect cavitation flow: Analyzing variations in silt mean diameter and concentration. *Powder Technology*, *356*, 671-690. https://doi.org/10.1016/j.powtec.2019.09.005

Hegde, M., Mohan, J., Warriaich, M. Q. M., Kavanagh, Y., Duffy, B., & Tobin, E. F. (2023). Cavitation erosion and corrosion resistance of hydrophobic sol-gel coatings on aluminium alloy. *Wear*, *524-525*, 204766. https://doi.org/10.1016/j.wear.2023.204766

Jin, H. Z., Liao, Z. Y., Zhou, J. F., Liu, X. F., Yao, H. C., & Wang, C. (2023). Study on the erosion characteristics of non-spherical particles in liquid-solid two-phase flow. *Journal of Applied Fluid Mechanics*, *16*(8), 1640-1653. https://doi.org/10.47176/jafm.16.08.1696

Kang, C., Liu, H. X., Song, L. B., & Zhang, S. (2021). *Cavitation erosion*. Science Press.

Koirala, R., Thapa, B., Neopane, H. P., & Zhu, B. S. (2017). A review on flow and sediment erosion in guide vanes of Francis turbines. *Renewable and Sustainable Energy Reviews*, *75*, 1054-1065. https://doi.org/10.1016/j.rser.2016.11.085

Krella, A., Tekumalla, S., & Gupta, M. (2020). Influence of micro Ti particles on resistance to cavitation erosion of Mg-xTi composites. *Mechanics of Materials*, *154*, 1037051. https://doi.org/10.1016/j.mechmat.2020.103705

Lin, P., Hu, D., Lin, Z. J., Liu, M. Q., Tang, C. L., & Wang, S. (2020). The mechanism of joint effects of axial-flow pump cavitation and sediment wear. *Advances in Mechanical Engineering*, *12*(5), 1-14. https://doi.org/10.1177/1687814020923066

Liu, S. H., Zhang, Y. W., & Tu, Y. L. (2016). Erosion wear law of coiled tubing outer wall. *China Powder Science and Technology*, *22*(6), 80-83. https://doi.org/10.13732/j.issn.1008-5548.2016.06.018

Lv, Y., Su, X., Yang, H., Zhang, J., Wang, R., & Zhu, Z. (2023). Velocity slip in a deep-sea slurry pump and its effect on particle transportation. *Journal of Applied Fluid Mechanics*, *16*(8), 1654-1665. https://doi.org/10.47176/jafm.16.08.1661

Menter, F. R. (1994). Two-equation eddy-viscosity turbulence models for engineering applications. *AIAA Journal*, *32*(8), 1598-1605. https://doi.org/10.2514/3.12149

Mueller, J. D. (2020). *Essentials of computational fluid dynamics*. CRC Press. https://doi.org/10.1201/b19471

Nurick, W. H. (1976). Orifice cavitation and its effect on spray mixing. *Journal of Fluid Engineering-Transactions of the ASME*, *98*, 681-687. https://doi.org/10.1115/1.3448452

Peng, C., Zhang, C. Y., Li, Q. F., Zhang, S. L., Su, Y., Lin, H. R., & Fu, J. H. (2021). Erosion characteristics and failure mechanism of reservoir rocks under the synergistic effect of ultrasonic cavitation and micro-abrasives. *Advanced Powder Technology*, *32*(11), 4391-4407. https://doi.org/10.1016/j.apt.2021.09.046

Peng, D. Q., Wang, Y. R., Hou, J. X., Yu, T. L., Wu, S. Y., & Wang, Z. P. (2021). Distribution and motion characteristics of ellipsoidal particles in liquid-solid two-phase flow in vertical upward pipe. *China Powder Science and Technology*, *27*(5), 94-104. https://doi.org/10.13732/j.issn.1008-5548.2021.05.012

Ranade, V. V., Bhandari, V. M., & Nagarajan, S. (2022). *Hydrodynamic cavitation-devices, design and applications*. Wiley-Vch. https://doi.org/10.1002/9783527346448

Romero, R., Teran, L. A., Coronado, J. J., Ladino, J. A., & Rodriguez, S. A. (2019). Synergy between cavitation and solid particle erosion in an ultrasonic

tribometer. *Wear*, *428-429*, 395-403. https://doi.org/10.1016/j.wear.2019.04.007

Saffman, P. G. (1965). The lift on a small sphere in a slow shear flow. *Journal of Fluid Mechanics*, *22*, 385-400. https://doi.org/10.1017/S0022112065000824

Schaeffer, D. G. (1987). Instability in the evolution equations describing incompressible granular flow. *Journal of Differential Equations*, *66*(1), 19-50. https://doi.org/10.1016/0022-0396(87)90038-6

Song, J. C., Zhang, M. X., LIN, L. Y., Li, Q. Q., Zeng, C., & Qiu, J. (2016). Research on erosion of particles to pipeline elbow based on computational fluid dynamics. *China Powder Science and Technology*, *22*(1), 1-5. https://doi.org/10.13732/j.issn.1008-5548.2016.01.001

Spalart, P. R. (2009). Detached-eddy simulation. *Annual Review of Fluid Mechanics*, *41*, 181-202. https://doi.org/10.1146/annurev.fluid.010908.165130

Stella, J., & Alcivar, R. (2019). Influence of addition of microsized alumina particles on material damage induced by vibratory cavitation erosion. *Wear*, 436-437, 203027. https://doi.org/10.1016/j.wear.2019.203027

Su, K. P., Xia, D. K., Wu, J. H., Xin, P., & Wang, Y. (2023). Particle size distribution effects on cavitation erosion in sediment suspensions. *Wear*, *518-519*, 204629. https://doi.org/10.1016/j.wear.2023.204629

Sun, J., Ge, X. F., Zhou, Y., Liu, D. M., Liu, J., Li, G. Y., & Zheng, Y. (2023). Research on synergistic erosion by cavitation and sediment: A review. *Ultrasonics Sonochemistry*, 95, 106399. https://doi.org/10.1016/j.ultsonch.2023.106399

Syamlal, M., Rogers, W., & O'Brien, T. J. (1993). *MFIX documentation*. National Technical Information Service.

Washio, S. (2014). *Recent developments in cavitation mechanisms*. Woodhead Publishing. https://doi.org/10.1016/C2013-0-18235-9

Xu, H. L., Chen, W., & Xu, C. (2019). Cavitation performance of multistage slurry pump in deep-sea mining. *AIP Advances*, *9*(10), 105024. https://doi.org/10.1063/1.5125800

Zhang, X. D., Zhang, W., Li, Z. T., Zhao, J., Liu, A. Z., & Li, H. Y. (2023). Numerical simulation and verification of the minimum fluidization velocity in a liquid-solid fluidized bed. *China Powder Science and Technology*, *29*(1), 80-89. https://doi.org/10.13732/j.issn.1008-5548.2023.01.009

Zhao, W. G., Han, X. D., Li, R. N., Zheng, Y. J., & Wang, Y. Y. (2017a). Effects of size and concentration of silt particles on flow and performance of a centrifugal pump under cavitating conditions. *Modern Physics Letters B*, *31*(34), 1750312. https://doi.org/10.1142/S0217984917503122

Zhao, W. G., Han, X. D., Sheng, J. P., & Pan, X.W. (2017b). Research on the effects of silt mean diameters and silt concentrations on the cavitation flow in a nozzle. *Journal of Shanghai Jiaotong University*, *51*, 1399-1404 (in Chinese). https://doi.org/10.16183/j.cnki.jsjtu.2017.11.017

Zhou, Q., Jiang, C. B., Cui, K. D., Ding, J. P., Chen, W., Chen, S. Z., & Guo, J. J. (2020). Experimental and numerical investigation on effect of inclined distributor on hydrodynamic characteristics of a bubbling fluidized bed. *China Powder Science and Technology*, 26(2), 13-19. https://doi.org/10.13732/j.issn.1008-5548.2020.02.003

Zhu, Z. C., Li, Y., & Lin, Z. (2023). *Solid-liquid two-phase flow in centrifugal pump*. Springer Nature. https://doi.org/10.1007/978-981-99-1822-5

Zwart, P. J., Gerber, A. G., & Belamri, T. (2004). *A two-phase flow model for predicting cavitation dynamics*. ICMF 2004 International Conference on Multiphase Flow, Yokohama.